

## Nonlinear Dynamics in a Coupled Vegetation–Atmosphere System and Implications for Desert–Forest Gradient

NING ZENG

*Department of Meteorology and Earth System Science Interdisciplinary Center, University of Maryland at College Park, College Park, Maryland*

KATRINA HALES AND J. DAVID NEELIN

*Department of Atmospheric Sciences and Institute of Geophysics and Planetary Physics, University of California, Los Angeles, Los Angeles, California*

(Manuscript received 28 January 2002, in final form 4 June 2002)

### ABSTRACT

Although the global vegetation distribution is largely controlled by the large-scale climate pattern, the observed vegetation–rainfall relationship is also influenced by vegetation feedback and climate variability. Using a simplified coupled atmosphere–vegetation model, this work focuses on the effects of these on the gradient of desert–forest transition. A positive feedback from interactive vegetation leads to a wetter and greener state everywhere compared to a state without vegetation. As a result, the gradient in vegetation and rainfall is enhanced at places with moderate rainfall. Climate variability is found to reduce vegetation and rainfall in higher rainfall regions, while enhancing them in lower rainfall regions, thus smoothing out the desert–forest gradient. This latter effect is due to the nonlinear vegetation response to precipitation and it is particularly effective in the savanna regions. The analyses explain results from a three-dimensional climate model. The results suggest that in a varying environment, vegetation plays an active role in determining the observed vegetation–rainfall distributions.

### 1. Introduction

A prominent feature in the spatial distribution of precipitation and vegetation in West Africa is the transition from the tropical rain forest in the Guinea Coast to the sandy desert of the Sahara over a distance of a little more than 1000 km (Fig. 1). Many other regions such as southern Africa also show similarly large gradients, especially around the savanna regions.

The desert–savanna transition in West Africa has been shown to vary widely on interannual timescales, as indicated by the movement of a desert–savanna boundary (Ellis and Swift 1988; Tucker et al. 1991; Goward and Prince 1995; Nicholson et al. 1998; Tucker and Nicholson 1999). The sensitivity of such transition zones to climate variability and anthropogenic disturbances has been demonstrated in a number of model studies (e.g., Charney 1975; Folland et al. 1986; Xue and Shukla 1993; Claussen et al. 1998; Zeng et al. 1999, hereafter ZNLT). Strong positive vegetation feedback can lead to multiple equilibria in the savanna regions (Claussen 1994; Claussen et al. 1998; Brovkin et al. 1998) but the

multiple equilibria can be destroyed by climate variability (Zeng and Neelin 2000, hereafter ZN).

Empirical analyses of the vegetation–atmosphere relationship show that vegetation distribution is largely controlled by the broadscale climate pattern (Holdridge 1947; Lieth 1975; Woodward 1987). For instance, the gradient in the West Africa desert–forest transition is largely set up by the dynamics of the African monsoon and the adjacent subtropical high pressure system. However, since vegetation provides a feedback to the atmosphere by modifying surface fluxes of energy, water, momentum, and chemical elements, the observed rainfall–vegetation relationship is a result of the interaction between climate and vegetation.

This paper aims to analyze the role of vegetation dynamics and climate variability on the spatial distribution of vegetation and rainfall in a tropical–subtropical environment. One goal is to explain the findings related to the role of climate variability in ZN using a simplified atmospheric model to represent rainfall response to vegetation change. Of particular relevance in terms of simple coupled vegetation–atmosphere modeling is the work of Brovkin et al. (1998), which discussed a multiple equilibrium regime also found in ZN, who used a three-dimensional atmospheric model and a simple vegetation model. While Brovkin et al.

---

*Corresponding author address:* Dr. Ning Zeng, Dept. of Meteorology and Earth System Science Interdisciplinary Center, University of Maryland at College Park, College Park, MD 20742.  
E-mail: zeng@atmos.umd.edu

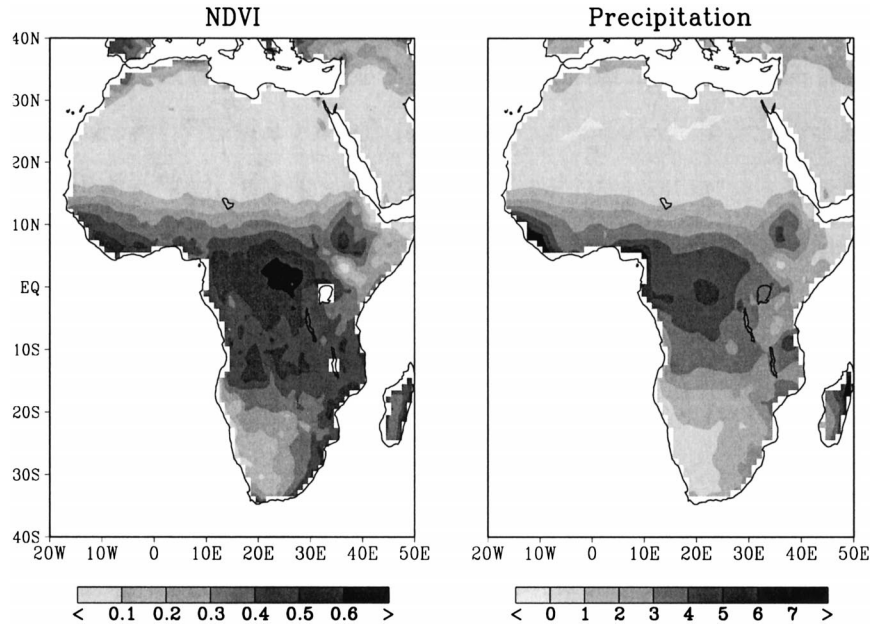


FIG. 1. Annual average of the normalized difference vegetation index (NDVI; Tucker and Nicholson 1999) and rainfall (New et al. 1999) over Africa, showing the large gradient from the forested Guinea Coast to the Sahara Desert.

focused on steady-state behaviors, ZN studied the effects of sea surface temperature (SST) induced climate variability on the stability of these multiple equilibria. Because of the uncertainties in our quantitative description of the vegetation–rainfall relationship, the vegetation model used in ZN will be compared to a formulation based on the Miami model [Lieth 1975; section 6 (this paper)] as well as a simpler model (appendix B) to highlight the mechanism.

## 2. A coupled vegetation–atmosphere model

We consider a simple coupled vegetation–atmosphere system with external forcing:

$$\frac{dV}{dt} = \frac{V^*(P) - V}{\tau_v} \quad (1)$$

$$P = \max[P_1 + \mu V + F(t), 0], \quad (2)$$

where  $V$  is vegetation;  $P$  is precipitation;  $t$  is time;  $\tau_v$  is the vegetation growth or loss timescale;  $P_1$ ,  $\mu$ , and  $V^*$  are the parameters and function describing the interaction between  $V$  and  $P$  discussed below; the function  $\max$  prevents  $P$  from becoming negative; and  $F(t)$  is a time-dependent forcing representing climate variability external to the coupled vegetation–atmosphere system such as that caused by SST variations.

The vegetation equation (1) is similar to the biomass equation used in various dynamic vegetation models (Shugart 1984; Ji 1995; Foley et al. 1996; Dickinson et al. 1998; Brovkin et al. 1998; ZNLT). At low latitudes, especially the tropical and subtropical seasonally wet

and dry regions, rainfall is the major factor in determining the vegetation distribution. We thus consider only the influence of rainfall, but not temperature and nutrients. Following ZN, we use a simple nonlinear function to describe equilibrium vegetation dependence on precipitation:

$$V^*(P) = \frac{P^a}{P^a + P_0^a}, \quad (3)$$

where  $a$  is an exponent parameter and  $P_0$  is a scaling precipitation. The empirically based Miami model (Lieth 1975) will be discussed in section 6.

It is also possible to consider the time evolution of precipitation in a way similar to (1):

$$\frac{dP}{dt} = \frac{P^*(V) - P}{\tau_p} + F(t). \quad (4)$$

However, since precipitation is highly nonlocal and mainly determined by large scale atmospheric circulation, it is difficult to link the above form more precisely with 3D atmospheric dynamics. Because the atmospheric response time ( $\tau_p$ ) to a heat anomaly is typically on the order of 1 month, much shorter than the vegetation timescale  $\tau_v$  and the interannual to interdecadal time-scales of interest here, we simply use an equilibrium relation (2). Brovkin et al. (1998) also discussed an equation similar to (4), and cautioned against using it.

The reason that the precipitation dependence on vegetation can be represented as a linear term [the  $\mu V$  term in (2)] is because the broadest-scale precipitation pattern is determined by geographical and climatological fac-

tors other than vegetation dynamics, so that in most cases vegetation change provides a relatively small perturbation to the broadscale precipitation distribution. Thus a linearization on this “basic state” leads to a good approximation of vegetation feedback on precipitation. The linearization coefficient  $\mu$  can be estimated theoretically (Zeng and Neelin 1999; ZNLT), or by studying atmospheric model sensitivity to surface vegetation property change. Thus, we are dealing with a regime where large change in vegetation leads to only small change in precipitation, while the typical range in precipitation differences leads to large vegetation change (appendix A).

The parameter  $P_1$  in (2) represents the large-scale atmospheric control on precipitation in the absence of vegetation ( $V = 0$ ). In the case of surface vegetation change, a rigorous derivation based on atmospheric dynamics (Zeng and Neelin 1999) links a parameter like  $P_1$  with large-scale atmospheric moisture convergence (with a unit conversion factor). The parameter  $P_1$  is a function of geographical location. In the case where moisture convergence is positive,  $P_1$  can be understood as the rainfall on a hypothetical planet where the land surface boundary is fixed to desert surface properties everywhere ( $V = 0$ ). For instance, if one takes a longitudinal transect in West Africa along the Greenwich meridian from the Guinea Coast to the Sahara (Fig. 1),  $P_1$  decreases from about 4 mm day<sup>-1</sup> to some negative value. Negative values of  $P_1$  corresponds to negative moisture convergence; that is, the large-scale atmospheric motion aloft is subsiding with divergence in the lower troposphere. When  $P_1$  is sufficiently negative, the large-scale atmospheric conditions prevent rainfall even when vegetation is present. Precipitation cannot be negative, hence the ramp-function nonlinearity represented by the max function in (2).

Strictly speaking, the observed rainfall gradient is  $P_1$  plus the contribution from vegetation feedback and climate variability (see next section). The gradient in  $P_1$  may or may not vary linearly as a function of geographical distance, depending on the atmospheric circulation characteristics. The precise value of  $P_1$  as a function of geographical distance can be estimated running an atmospheric model with the land surface boundary fixed as desert ( $V = 0$ ) everywhere. In this paper, we consider the modification of a given gradient in  $P_1$ , regardless of the origin of this initial gradient, but bearing in mind that the observed gradient such as that from Guinea Coast to the Sahara in West Africa is an approximation of  $P_1$ .

In (1) and (2), we normalize time by vegetation timescale  $\tau_v$ ; and  $P$ ,  $\mu$ , and  $F$  by  $P_0$  such that

$$\begin{aligned} t &\rightarrow t/\tau_v & P &\rightarrow P/P_0 & \mu &\rightarrow \mu/P_0 \\ F &\rightarrow F/P_0 & V &\rightarrow V. \end{aligned}$$

Here  $V$  can be interpreted as a normalized leaf area index (LAI) as (ZNLT)

$$V = \text{LAI}/\text{LAI}_{\max}, \quad (5)$$

where  $\text{LAI}_{\max}$  is a maximum LAI typically of value 8. Hereafter we use the symbols  $t$ ,  $P$ ,  $\mu$ , and  $F$  for the normalized dimensionless variables unless otherwise stated.

Substituting  $V^*$  in (1) using (3), we obtain a set of dimensionless equations:

$$\frac{dV}{dt} = \frac{P^a}{P^a + 1} - V \quad (6)$$

$$P = \max\left[P_1 + \mu V + F_0 \sin\left(\frac{2\pi}{T}t\right), 0\right]. \quad (7)$$

In this paper we consider only periodic forcing with adjustable amplitude  $F_0$  and period  $T$ .

Based on the literature (e.g., Lieth 1975) and our own analysis, the scaling rainfall is taken as  $P_0 = 3$  mm day<sup>-1</sup>. Thus a forcing amplitude of  $F_0 = 1$  corresponds to 3 mm day<sup>-1</sup>. Based on the dimensionless equations, our analyses do not directly refer to physical values that are nonetheless important in connecting the model results to real situations. The parameter  $\mu$  represents the coupling strength of the two-way interaction of  $V$  and  $P$ , and it is the equivalent of  $\alpha\mu$  of ZNLT multiplied by a location-dependent factor. By examining the interdecadal difference between a fixed vegetation model run and an interactive vegetation run (Fig. 2 of ZNLT) we estimated that  $\mu = 0.5$ . Further details are discussed in appendix A. Vegetation processes tend to have multiple timescales, ranging from minutes for leaf level gas exchange to several decades for forest succession (Pielke et al. 1998), but in the current context the most relevant are the slower timescales. Since time is normalized by the vegetation timescale  $\tau_v$  in our model, the results found here are scalable to different timescales as long as the physical assumptions made are valid.

### 3. Results for the Zeng–Neelin model

#### a. The coupled system in steady state without external forcing

Steady-state solution of above equations (6)–(7) with  $F = 0$  is given by setting  $dV/dt = 0$ :

$$V = V^*(P) = \frac{P^a}{P^a + 1} \quad (8)$$

$$P = P^*(V) = \max[P_1 + \mu V, 0]. \quad (9)$$

This is illustrated in Fig. 2a. In the first quadrant where both  $P$  and  $V$  are positive, there is one solution at  $P_s = 1.09$ ,  $V_s = 0.59$  for the standard parameter values  $\mu = 0.5$ ,  $a = 4$ , and  $P_1 = 0.8$  (Fig. 2a, marked by a star; we use  $P_s$  and  $V_s$  to denote the steady-state solution). Without vegetation feedback (land surface is like desert everywhere), the steady-state solution is significantly drier and less green ( $P_s = 0.80$ ,  $V_s = 0.29$  for  $\mu = 0$ , marked by a triangle).

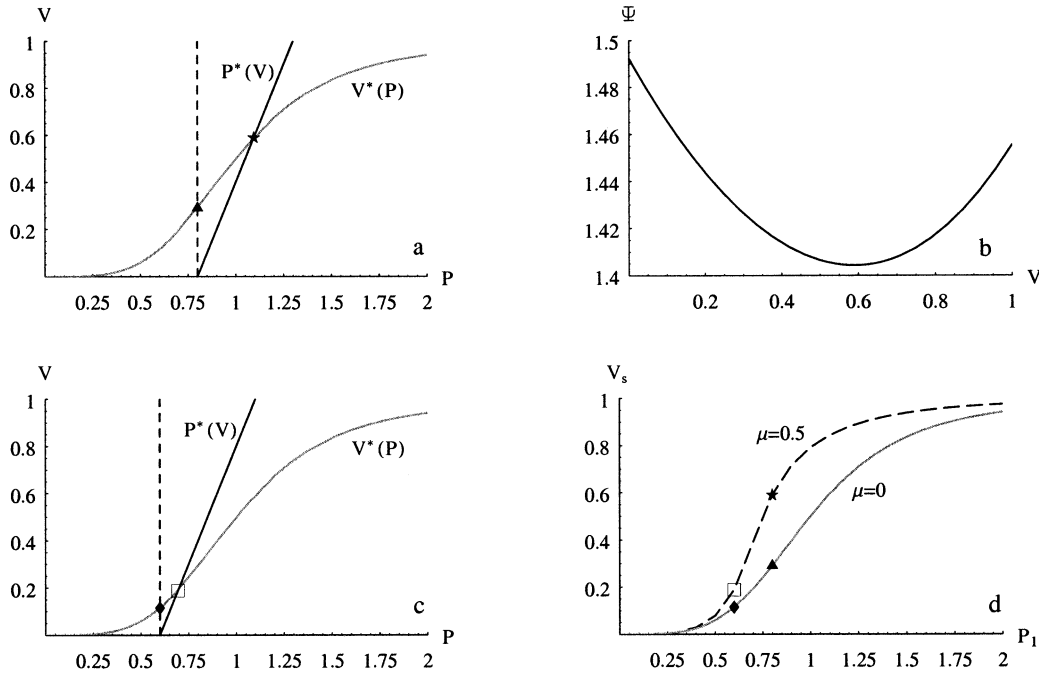


FIG. 2. Vegetation feedback effects without forcing: (a) steady-state vegetation response curve to prescribed precipitation  $V^*(P)$  [Eq. (8), gray solid line]; precipitation response to vegetation  $P^*(V)$  at  $\mu = 0.5$ ,  $a = 4$ , and  $P_1 = 0.8$  [Eq. (9), solid line];  $P^*(V)$  at  $\mu = 0$  and  $P_1 = 0.8$  (no vegetation feedback, dashed line); the steady-state solution of the coupled equation in each case is marked by a star and a triangle; (b) the potential function  $\Psi(V)$  with  $\mu = 0.5$  and  $P_1 = 0.8$ ; (c) as in (a) but for  $P_1 = 0.6$ ; (d)  $V_s$  as a function of  $P_1$  for  $\mu = 0$  (gray solid line; noninteractive vegetation:  $P_1$  is given by a hypothetical atmosphere with the land surface boundary fixed like desert everywhere) and  $\mu = 0.5$  (dashed line; interactive vegetation); for the noninteractive case, the  $V_s(P_1)$  curve is identical to the  $V^*$  curve in (a) and (c).

A useful tool is the potential function  $\Psi(V)$  defined such that (Brovkin et al. 1998)

$$\frac{dV}{dt} = -\frac{\partial\Psi}{\partial V}. \quad (10)$$

Substitute (9) into (6) and integrate with respect to  $V$ :

$$\Psi = \int -\left[ \frac{(P_1 + \mu V)^a}{(P_1 + \mu V)^a + 1} - V \right] dV. \quad (11)$$

The potential function  $\Psi$  as a function of  $V$  is plotted in Fig. 2b. The minimum of  $\Psi$  corresponds to the steady-state solution ( $P_s, V_s$ ). We note that this potential can be defined because this is a one-variable system; it would not necessarily generalize to a Lyapunov function for higher dimensional versions of this system. The potential can also be time varying, in which case the slope  $-(\partial\Psi/\partial V)$  still allows  $dV/dt$  to be visualized but minima of  $\Psi$  do not correspond to steady states.

Figure 2c shows the case for  $P_1 = 0.6$  illustrating the solutions with and without vegetation feedback for a region where large-scale conditions are less favorable to precipitation. Figure 2d shows the steady-state solution value of  $V_s$  as a function of  $P_1$  for  $\mu = 0$  and  $\mu = 0.5$ . As discussed above, the gradient in  $P_1$  represents a gradient in large-scale atmospheric circulation control on precipitation. The  $P_1$  gradient is not necessarily a

linear function of geographic gradient. Without vegetation feedback ( $\mu = 0$ ), a linear gradient in  $P_1$  corresponds to a nonlinear gradient in  $V_s$ , due to the nonlinear response function (8). Vegetation feedback ( $\mu = 0.5$ ) enhances the vegetation distribution differently at different places, and the resulting precipitation  $P$  is no longer a linear function of  $P_1$  (not shown). Interestingly, the vegetation effect (difference between  $\mu = 0.5$  and  $\mu = 0$ ) is largest at intermediate values of  $P_1$ . This is because at low  $P_1$ , there is nearly no vegetation, and thus little feedback on climate, while at high  $P_1$ , vegetation is nearly saturated ( $V_s \rightarrow 1$ ). As a result, the desert–forest gradient is enhanced mostly at intermediate values of  $P_1$ . Therefore the climate of semidesert to woodland regions may have the largest response to vegetation feedback.

#### b. Sensitivity to forcing amplitude

Natural and anthropogenic climate variability occur on multiple timescales. On interannual to interdecadal timescales of concern here, much of this variability arises from interactions among other components of the climate system such as ocean and atmosphere; we therefore treat the variability as an external forcing for the coupled vegetation–atmosphere system.

If one assumes vegetation timescale  $\tau_v = 1$  yr, then

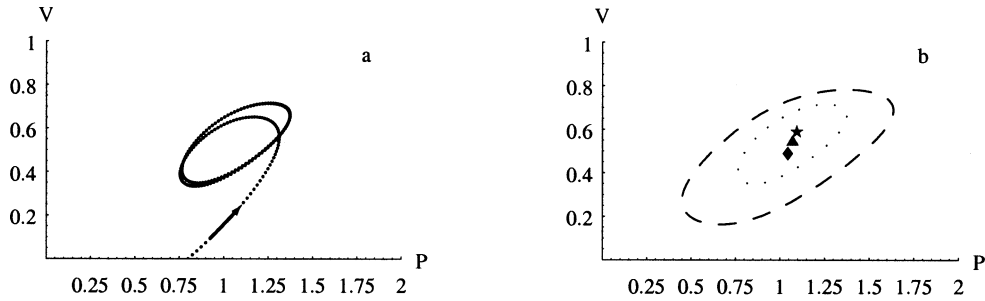


FIG. 3. Trajectory of the time evolution in the phase space of  $(P, V)$  with periodic forcing: (a) evolution toward a limit cycle; (b) the final limit cycle for three different forcing amplitudes:  $F_0 = 0$  (the averages  $\bar{P}$  and  $\bar{V}$  are marked by a star),  $F_0 = 0.25$  (dotted line,  $\bar{P}$  and  $\bar{V}$  marked by a triangle), and  $F_0 = 0.5$  (dashed line, averages marked by a diamond); using standard parameter values:  $P_1 = 0.8$ ,  $\mu = 0.5$ ,  $T = 6$ .

a forcing period  $T = 6$  corresponds to 6 yr, a timescale between that of El Niño and the decadal scale at which there is strong variability in the Tropics (Federov and Philander 2000). An amplitude of  $F_0 = 0.5$  corresponds to peak to peak rainfall variation of  $3 \text{ mm day}^{-1}$ , somewhat larger than typical variability in the Tropics. These values are used in our standard case. At these parameter values, a phase plot in Fig. 3a shows the time evolution toward a final cyclical orbit. Each cycle corresponds to the period of the forcing. The initial state is  $P = 0.5$  and  $V = 0$ . The orbit settles onto the limit cycle very rapidly, within a time of about  $6\tau_v$ .

When the forcing amplitude increases, both  $V$  and  $P$  decrease, as shown in Fig. 3b. Of importance are the

average values over a limit cycle that we denote as  $\bar{V}$  and  $\bar{P}$  (shown as markers in Fig. 3b). Most interestingly,  $\bar{V}$  has decreased from 0.59 to 0.54 to 0.49 when  $F_0$  increases from 0 to 0.25 to 0.5. This apparent “drift” in the averages of  $\bar{V}$  and  $\bar{P}$  is a “rectifier” effect due to the interaction of the periodic forcing and the nonlinearity in the system; that is, the nonlinear dependence of vegetation growth tendency on precipitation  $V^*(P)$ .

Before addressing the precise mechanism (next section), we show in Fig. 4a additional cases with different forcing amplitudes. In each case, the average value  $\bar{V}$  is computed over the limit cycle, similar to Fig. 3b, and is plotted as dots, while the maximum and minimum values over a limit cycle are plotted as connected lines.

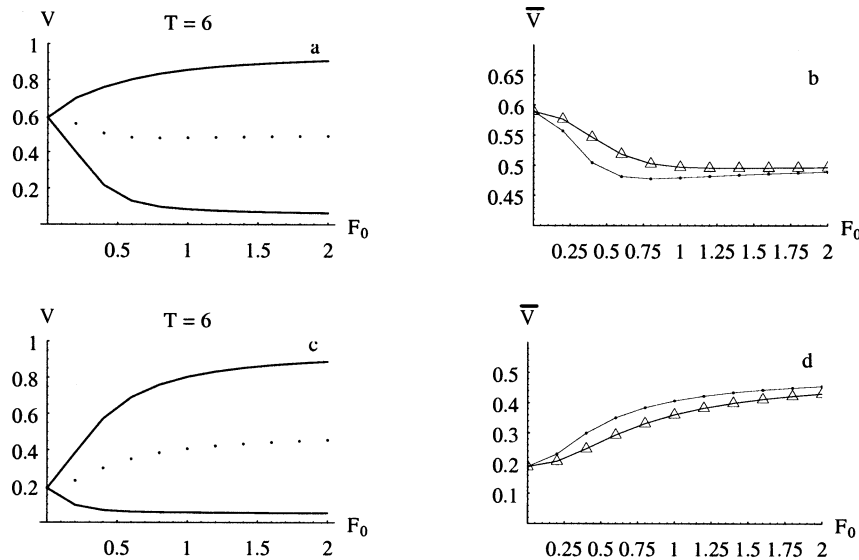


FIG. 4. Vegetation as a function of forcing amplitude for two values of  $P_1$ : (a)  $\bar{V}$  (average over a limit cycle; dotted line),  $V_{\max}$  (max value over a limit cycle; upper solid line), and  $V_{\min}$  (min value over a limit cycle; lower solid line), for  $P_1 = 0.8$ ,  $\mu = 0.5$ ,  $T = 6$ ; (b)  $\bar{V}$  as in (a) (linked dots) and  $\bar{V}$  for the case where the feedback from  $V$  is fixed at its steady-state value  $V = 0.59$  in Eq. (7) (linked triangles), for  $P_1 = 0.8$ ,  $\mu = 0.5$ ,  $T = 6$ ; (c)  $\bar{V}$  (average over a limit cycle; dotted line),  $V_{\max}$  (max value over a limit cycle; upper solid line), and  $V_{\min}$  (min value over a limit cycle; lower solid line), for  $P_1 = 0.6$ ,  $\mu = 0.5$ ,  $T = 6$ ; (d)  $\bar{V}$  as in (c) (linked dots) and  $\bar{V}$  for the case where the feedback from  $V$  is fixed at its steady-state value  $V = 0.19$  in Eq. (7) (linked triangles), for  $P_1 = 0.6$ ,  $\mu = 0.5$ ,  $T = 6$ .

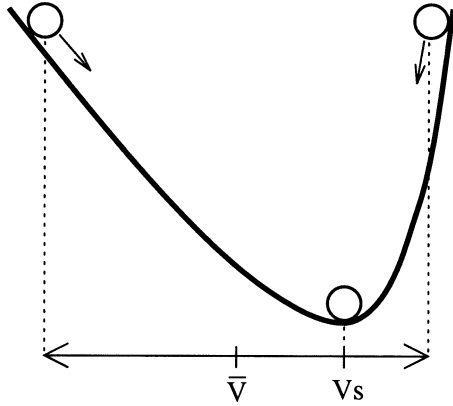


FIG. 5. Schematic diagram of an asymmetric potential function: because of the steeper wall on the right, the oscillatory orbit has an average position  $\bar{V}$  to the left of the steady-state position  $V_s$ . This is an exaggerated version of Fig. 2b, corresponding to the convex part of Fig. 2a. The asymmetry is reversed with a steeper wall on the left for the concave part of  $V^*(P)$  as in the case of Fig. 2c.

Figure 4b shows a zoom-in view of  $\bar{V}$  as a function of  $F_0$  (lower curve). The  $\bar{V}$  drops from 0.59 at  $F_0 = 0$  to 0.48 at  $F_0 = 0.75$ , and increases somewhat at larger  $F_0$ . This is because  $P$  cannot be negative, so it stays at zero during the part of the cycle when forcing is extremely negative. The largest modification of  $\bar{V}$  relative to the  $F_0 = 0$  case is about 0.1. This corresponds to a change in LAI of 0.8 (assume  $V$  is proportional to LAI with a maximum LAI of 8).

In section 3a we discussed the positive vegetation feedback in enhancing rainfall. In order to see this feedback effect (not the direct nonlinear response) in this nonlinear drift, the upper curve in Fig. 4b was computed with  $V$  in (7) fixed at its steady-state value (so the two curves overlap at  $F_0 = 0$ ). The difference in the two curves is the contribution to this nonlinear drift from vegetation feedback. This effect might be too subtle to discern in observations but could be evaluated in other climate models.

When  $P_1$  is small, the drift is toward a “wetter” and “greener” state (Figs. 4c,d). This is due to the different sign of the curvature of the  $V^*(P)$  curve (see Fig. 2c) in the vicinity of the steady solution. We now turn to the mechanism of the nonlinear drift and the difference at low and high  $P_1$  values.

### c. Mechanism of the nonlinear drift

The nonlinear drift in the equilibrium mean state can be understood most easily using the potential function  $\Psi(V)$ . Because of the nonlinearity, the potential well is asymmetric (Fig. 5), with the right wall steeper than the left wall. Without forcing, the steady state is at the very bottom of the well ( $V = V_s$ ). But as soon as the system is forced to oscillate, it tends to spend less time on the steeper right slope, because it is pulled back toward the bottom more strongly. Thus the average position is shift-

ed to the gentler side of the potential well. One cautionary reminder in interpreting Fig. 5 is that the correct mechanical analog is overdamped (highly frictional) motion in a potential well because Eq. (6) is a first-order differential equation, so that the rhs corresponds to velocity, not acceleration.

Figure 5 also highlights that the direction of the drift depends on the shape of the nonlinearity. If  $V^*(P)$  is convex shaped [more precisely, the second derivative of  $V^*(P)$  is negative, as in Fig. 2a at large  $P_1$ ], the drift reduces vegetation, as seen in Figs. 4a,b. If  $V^*(P)$  is concave shaped [the second derivative of  $V^*(P)$  is positive, as in Fig. 2a at small  $P_1$ ], the drift is toward increased vegetation, as seen in Figs. 4c,d.

When the periodic forcing is a small perturbation ( $F_0$  small), the drift in the mean state as a linearization can be analytically computed. This is done for the simpler case of the Miami model (section 6). A system exhibiting similar nonlinear drift behavior is also discussed in appendix B. Because of the simpler cubic nonlinearity, the full nonlinear drift can be demonstrated analytically in that system.

### d. Sensitivity to forcing period and relation to linear model

In our simple vegetation–atmosphere system, vegetation has a single timescale  $\tau_v$ . Although vegetation processes tend to have multiple timescales (Pielke et al. 1998), what matters in our simplified system is the relative temporal scale between vegetation response and forcing. Figure 6a shows the limit cycles for  $T = 1, 6$ , and 50 with other parameters taking their standard values ( $F_0 = 0.5, P_1 = 0.8, \mu = 0.5$ ). As forcing period  $T$  increases, the response in both  $V$  and  $P$  increases, because at fast forcing vegetation (and its feedback on precipitation) simply cannot change fast enough, while it can adjust toward a near steady state at the slow forcing limit. When  $T$  approaches infinity (i.e., the forcing is very slow), the curve approaches the steady-state response curve  $V^*(P)$ .

Figure 6b shows  $\bar{V}, V_{\max}$ , and  $V_{\min}$  as a function of forcing amplitude  $F_0$  at a fast forcing  $T = 1$ . The most noticeable difference is that the amplitude of the oscillation in the vegetation response is much smaller compared to the  $T = 6$  case in Fig. 4a because of the slow vegetation response. However, precipitation still has a large amplitude (not shown), because the contribution from vegetation feedback through the  $\mu V$  term is much smaller compared to the forcing that contributes to  $P$  directly.

Because of the  $2\pi$  factor resulting from the assumed sinusoidal forcing,  $T = 2\pi \approx 6$ , not  $T = 1$ , is the forcing timescale comparable to the vegetation timescale. Interestingly, the mean value  $\bar{V}$  for the  $T = 1$  case is similar to the  $T = 6$  case (Fig. 4a), in agreement with the visual impression of Fig. 6a. At  $T = 50$  (not shown), a significant difference occurs in  $\bar{V}$  for  $F_0$  less than or

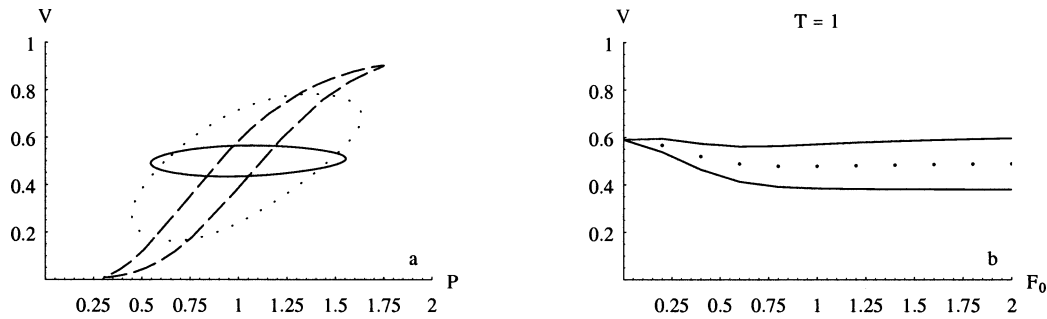


FIG. 6. (a) Phase diagram at  $T = 1$  (solid line),  $T = 6$  (dotted line), and  $T = 50$  (dashed line) for  $P_1 = 0.8$ ,  $\mu = 0.5$ ,  $F_0 = 0.5$ ; (b) as in Fig. 4a, but for  $T = 1$ .

on the order of 0.5, reasons for which are discussed in section 6.

The dependence of response amplitude on the forcing period is fundamentally a linear response, although modified by nonlinearity when the forcing is large. This dependence has implications for the vegetation response to climate variability on different timescales, as discussed in a linearized version of the present model (ZNL). The relation between the nonlinear and the linear model, as well as the analytical solution of the linear model are discussed in appendix A.

#### 4. Implications for desert–forest transition gradient

The parameter  $P_1$  in (9) can be interpreted as a large-scale atmospheric control (moisture convergence) on precipitation in the absence of vegetation [ $V = 0$  in Eq. (9)]. For instance, as noted in section 2, along a transect in West Africa following the Greenwich meridian from the Guinea Coast to the Sahara (Fig. 1),  $P_1$  decreases from about  $4 \text{ mm day}^{-1}$  to some negative value (but  $P$  cannot be negative). This is illustrated in Fig. 7 where the regions represented by A, B, C increase in aridity.

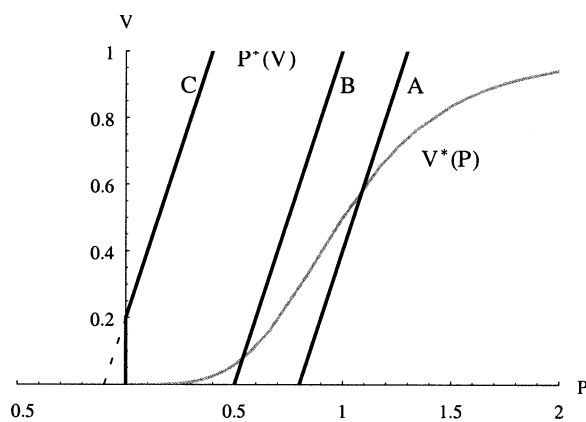


FIG. 7. Precipitation dependence on vegetation  $P^*(V)$  for three regions along a forest–desert gradient in the absence of atmospheric variability: aridity increases from region A to region C as characterized by decreases in the parameter  $P_1$ .

These represent a state without climate variability, and C is a region with negative  $P_1$  (large-scale moisture divergence).

In the presence of climate variability, as the result of the nonlinear drift discussed in the previous section, region A becomes drier because of the convex-shaped nonlinearity above the inflection point, and Region B becomes wetter because of the concave-shaped nonlinearity below the inflection point. Region C presents a new case where the nonlinearity associated with positive precipitation is encountered. For instance, at the heart of the Sahara, there is strong atmospheric subsidence aloft and divergence at low level, corresponding to negative  $P_1$ , but precipitation is nearly zero. This introduces a strong nonlinearity as all the regions with  $P_1 < 0$  become degenerate at zero precipitation. As a consequence, climate variability would on average introduce a larger than zero rainfall in these regions. This is no surprise because even the driest regions in the world get some rainfall occasionally. Thus the driest regions become wetter and greener in the presence of climate variability. The ZN model and parameter values used here are such that the region C–like situation only shows a weak “greening” effect, but strong impacts are seen in the Miami model discussed in section 6.

The sinusoidal forcing representing climate variability is applied to each point along such a forest–desert transect (defined by a gradient in  $P_1$ ), and the distribution of the average vegetation  $\bar{V}$  is compared to the vegetation  $V_s$  in the case without forcing. Figure 8 shows the new vegetation distribution along such a  $P_1$  gradient. In the presence of climate variability, the originally drier regions become wetter and greener, while the originally wetter regions become drier and less green (Fig. 8). The sign change occurs at  $P_1 = 0.71$ , above which climate variability tends to reduce rainfall and vegetation, and below which it tends to increase them. The largest changes (Fig. 8b) occur only slightly above and below the inflection point ( $P = 1$ ). Thus the spatial gradient of rainfall and vegetation is smoothed mostly around the inflection point where intermediate vegetation cover, such as savanna, exists.

It is worth noting that the effect of climate variability

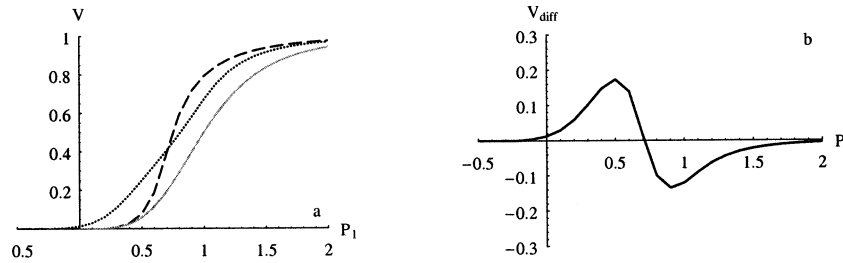


FIG. 8. Modification of desert–forest gradient by vegetation feedback and climate variability: (a) vegetation distribution along a desert–forest transect ( $P_1$  gradient): pure vegetation response to prescribed precipitation gradient in  $P_1$  [ $V^*(P)$  or  $V_s$  at  $\mu = 0$ ; solid gray line]; interactive vegetation with fixed climate  $F_0 = 0$  ( $V_s$  at  $\mu = 0.5$ ; dashed line); interactive vegetation with climate variability of amplitude  $F_0 = 0.5$  ( $\bar{V}$  at  $\mu = 0.5$ ; dotted line); the first two lines are identical to those in Fig. 2d. (b) Difference between cases with and without climate variability [ $\bar{V} - V_s$ , dotted line minus dashed line in (a)].

acts in combination with the vegetation feedback effect: in the absence of climate variability, a positive vegetation feedback tends to enhance the desert–forest gradient (compare the gray solid line with the dashed line in Fig. 8a) while the effect of climate variability is to reduce this gradient. The positive vegetation feedback effect is most effective at intermediate  $P_1$  (grass–woodland region) while the variable climate effect is most effective in the low  $P_1$  and intermediate  $P_1$  range but with opposite sign.

**5. ZN model in the multiple equilibrium regime**

The nonlinearity in the vegetation response to precipitation allows the existence of multiple equilibrium steady states in the coupled system as demonstrated by a number of modeling results (Claussen 1994; Brovkin et al. 1998; ZN), although details and the precise mechanisms can differ. In the ZN model coupled to either an intermediate-complexity climate model (ZN) or to the current simple atmospheric feedback, multiple equilibria may exist when the vegetation response to precipitation is very strong. The criterion requires that  $P_1$  is within an intermediate range, and more importantly, the slope of  $P^*(V)$  (i.e.  $\mu$ ) is larger than the slope of the  $P^*(V)$  curve at its inflection point (i.e.,  $P = 1$ ):

$$\mu > a/4. \tag{12}$$

Thus, at  $a = 4$ , the necessary condition for multiple equilibria is  $\mu > 1$ .

The graphical representation of the steady-state solution in the  $P$ – $V$  plane and the potential function are shown in Fig. 9 for the case with  $F_0 = 0$  and for the cases corresponding to minimum and maximum forcing. The double minima of the potential function for the  $F_0 = 0$  case correspond to two stable solutions while the maximum in between corresponds to an unstable equilibrium solution. The high- $V$  stable solution for  $F_0 = 0$  is more stable than the low- $V$  solution. This is qualitatively similar to Brovkin et al. (1998). Over time the potential function changes according to the time-varying forcing. The dashed lines in Fig. 9b are the potential functions for the minimum and maximum forcing (lower and upper curves, respectively). The potential moves from having two minima solutions (lower dashed line and solid line in Fig. 9b) to a potential where only one minimum exists (upper dashed line in Fig. 9b, where forcing is largest) and back through the forcing period cycle. For a time-dependent potential, minima do not in general correspond to asymptotic solutions. The rate of change of  $V$  is given by the slope of the potential, so at a given time, solutions tend toward the minima but do not necessarily reach them.

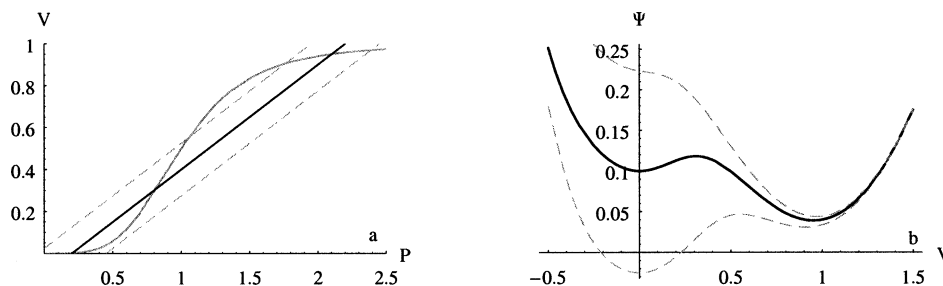


FIG. 9. As in Fig. 2 but for the ZN model with multiple equilibria: (a)  $V^*(P)$  (solid gray line),  $P^*(V)$  for no external forcing (solid line), and  $P^*(V)$  for min and max phases of oscillatory external forcing when  $F_0 = 0.25$  (dashed lines). (b) The potential function for no external forcing (solid line) and for min and max values of the periodic external forcing when  $F_0 = 0.25$  (dashed lines). Parameter values are  $P_1 = 0.2$ ,  $\mu = 2$ ,  $a = 4$ .

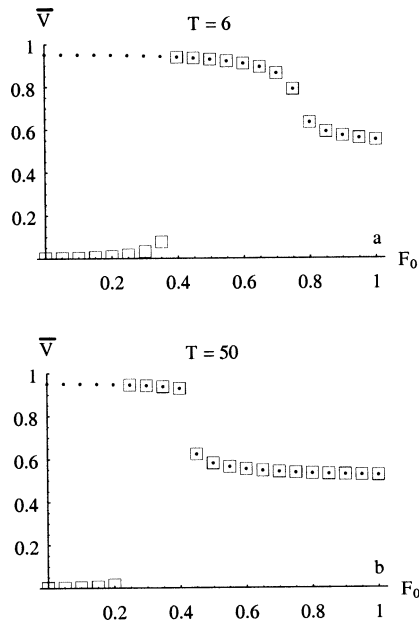


FIG. 10. ZN model with multiple equilibria:  $\bar{V}$  as function of  $F_0$  for two different initial conditions: dots are for high initial  $V$ , and open squares are for low initial  $V$ . Parameter values are  $P_1 = 0.2$ ,  $\mu = 2$ ,  $a = 4$ . (a)  $T = 6$ ; (b)  $T = 50$ .

Figure 10 shows the average value  $\bar{V}$  as a function of external forcing amplitude for two different forcing periods:  $T = 6$  and  $T = 50$ . The upper branch starts from an initial condition with  $V$  near 1 while the lower branch starts from  $V$  near 0. For small values of forcing amplitude two solution branches coexist similar to the  $F_0 = 0$  multiple equilibria. As forcing amplitude increases, the upper branch  $\bar{V}$  decreases, while the lower branch  $\bar{V}$  increases. This is because of the concave-shaped local nonlinearity at low  $P$  such that the nonlinear drift goes in the opposite direction of the upper branch where the nonlinearity is convex shaped. An analytical model with cubic nonlinearity is discussed in appendix B to further highlight this behavior.

This behavior of two multiple equilibria converging toward an intermediate state as forcing increases confirms the numerical results of ZN (their Fig. 4). However, in the present model the lower branch “jumps” to join the upper branch when forcing amplitude is only moderately large at  $F_0 = 0.4$  for  $T = 6$  and  $F_0 = 0.25$  for  $T = 50$ , unlike in ZN where the two branches are more or less symmetric. The jump occurs when forcing is large enough because for part of the cycle, the orbit amplitude is large enough to fall into the attractor of the upper branch that is more stable, as may be seen from the potential in Fig. 9b (upper dashed curve).

Comparing Figs. 10a and 10b, lower-frequency forcing allows the orbit to jump to the upper branch at lower forcing amplitude than higher-frequency forcing (cases  $T = 50$  and  $T = 6$ ). For long forcing periods, the vegetation has ample time to adjust to the varying forcing. Thus during the part of the cycle when the potential has

only one minimum, vegetation has time to move to the upper attractor. For higher-frequency forcing, in less than the time it takes vegetation to move to the upper branch, the forcing may have changed back into a regime with two minima in the potential. Thus it takes higher forcing amplitudes to push vegetation on to the upper attractor when forcing frequencies are higher. The same argument can be made for the second jump (seen at  $F_0$  approximately 0.4 in the  $T = 50$  case) from an orbit around the upper branch to a larger orbit that is alternately attracted to one of the minima of the potential and then the other.

We note that no jumps in  $\bar{V}$  were seen in the ZN 3D model. This is partly because they used a high value  $a = 64$  ( $a = 4$  here), which made the lower and upper branches more symmetric. Smoother behavior may also have occurred because of spatial dependence in the atmospheric response. Overall, in both the three-dimensional model and this prototype, as climate variability is increased, the possibility of having multiple equilibria is reduced.

In a univariate dynamical system, a discontinuous jump in stable solutions, such as that which occurs in the  $\bar{V}$  solution, would be associated with a saddle node bifurcation where one stable solution (the lower  $V$  solution) connects to the intermediate unstable solution. The upper branch remains as the sole stable solution, similar to a perturbed pitchfork bifurcation (see appendix B). Due to the time-dependent forcing, the present system is equivalent to a two-variable system. In terms of the orbits in a  $P$ - $V$  phase space, the behavior is continuous. Figure 11 shows orbits in this phase space for three values of the forcing amplitude for the  $T = 50$  case. For low forcing amplitude there are two stable orbits for differing initial conditions (in Fig. 11a). If one considers the limit of steady solutions for cases corresponding to the extremes of the external forcing (dashed lines in Fig. 11), for moderately large values of  $F_0$  there is no lower stable solution (Fig. 11b). In the periodic case, orbits on the lower branch are deformed as  $F_0$  increases until the forcing amplitude exceeds a critical value. Then an orbit that begins on the lower branch moves to the upper attractor during high forcing phases and cannot get back to the lower branch during low forcing phases, illustrated in Fig. 11b with  $F_0 = 0.25$ . When  $F_0$  exceeds another larger critical value ( $F_0 \approx 0.45$  for  $T = 50$  case and  $F_0 \approx 0.8$  for  $T = 6$  case)  $\bar{V}$  is reduced since now the orbit in phase space sweeps out a path that alternately tends toward each of the former equilibria, as in Fig. 11c. Although the behavior depends on the amplitude of the time-dependent forcing, much of the behavior can be understood in relationship to a univariate system, as outlined in appendix B.

## 6. Results for the Miami model

A number of simple relations for the vegetation response curve to precipitation  $V^*(P)$  have been proposed

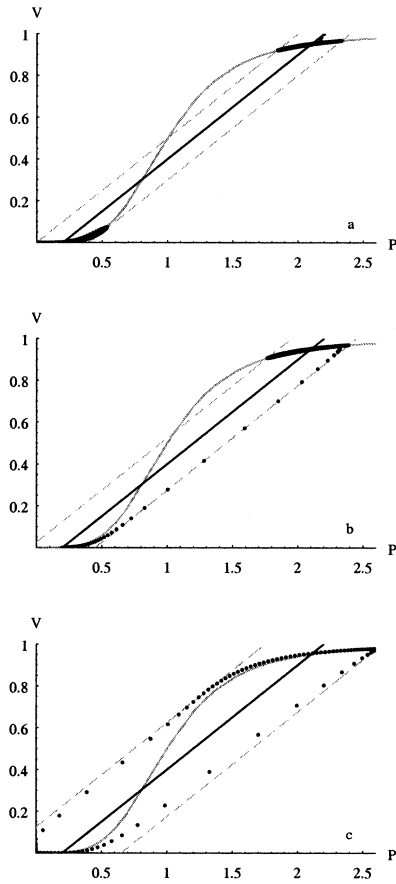


FIG. 11. Phase plots of  $P$  and  $V$  for (a) initial conditions  $V(0) = 0$  (lower orbit) and  $V(0) = 1$  (upper orbit) for  $F_0 = 0.2$ , (b)  $F_0 = 0.25$ , (c)  $F_0 = 0.45$ . Superimposed are curves for  $V^*(P)$  (gray),  $P^*(V)$  for zero forcing (solid), and the range of  $P^*(V)$  (dashed) for the given  $F_0$  (see caption of Fig. 9a). Parameter values are  $P_1 = 0.2$ ,  $\mu = 2$ ,  $a = 4$ , and  $T = 50$ .

(e.g., Lieth 1975; Brovkin et al. 1998; ZN). They were generally derived by empirically correlating spatially distributed data of precipitation and vegetation. To test the robustness of our findings, we also analyze the Miami model (Lieth 1975):

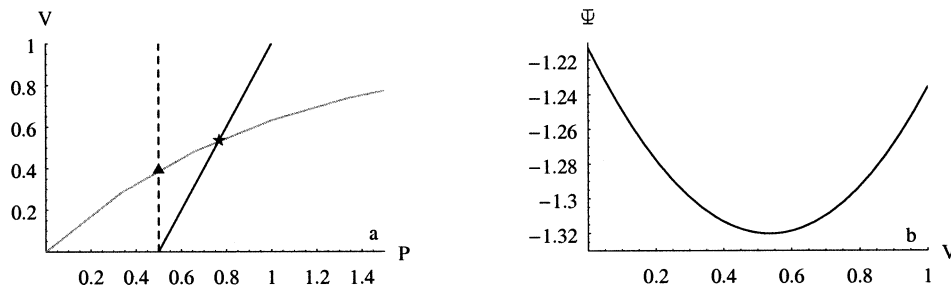


FIG. 12. As in Figs. 2a,b, but for the Miami model: (a) steady-state vegetation response curve to prescribed precipitation  $V^*(P)$  [Eq. (13), gray solid line]; precipitation response to vegetation  $P^*(V)$  at  $\mu = 0.5$  and  $P_1 = 0.5$  [Eq. (9), solid line];  $P^*(V)$  at  $\mu = 0$  and  $P_1 = 0.5$  (no vegetation feedback, dashed line); the steady-state solution of the coupled equation in each case is marked by a star and a triangle; (b) the potential function  $\Psi(V)$  for  $\mu = 0.5$  and  $P_1 = 0.5$ .

$$V^*(P) = 1 - e^{-P/P_0}. \tag{13}$$

Normalizing (13) by  $P_0$ , and using this in (1) one obtains a system:

$$\frac{dV}{dt} = 1 - e^{-P} - V \tag{14}$$

$$P = \max \left[ P_1 + \mu V + F_0 \sin \left( \frac{2\pi}{T} t \right), 0 \right]. \tag{15}$$

The steady-state solution in the  $P$ - $V$  plane and the potential function are shown in Fig. 12, which may be compared to the ZN model case in Fig. 2. Qualitatively, many aspects of the solution are similar although intermediate values of  $V$  occur for smaller values of  $P_1$ . We thus examine a slightly shifted parameter range in  $P_1$ . Figure 13 shows the average value  $\bar{V}$  as a function of external forcing amplitude at  $T = 6$ . In general, the behavior is qualitatively similar to the ZN model. In particular, the nonlinear drift (Fig. 13b) is toward a less vegetated, drier state, similar to the large  $P_1$  upper branch of the ZN model, as the Miami model  $V^*(P)$  curve is convex everywhere. The slight increase in  $\bar{V}$  for large  $F_0$  is again due to effects of the nonlinearity associated with positive-only precipitation for large variability.

When climate variability is applied as in the ZN model case (section 4), the Miami model shows a similar drying effect in high rainfall regions and increased rainfall in the low rainfall regions (Figs. 14, 15). However, a significant difference between the two models is the behavior in the low rainfall regions, such as regions B and C in Fig. 14. In the Miami model, the largest enhancement due to the variable forcing occurs around  $P_1 = 0$  at a much drier place than in the ZN model. As discussed in section 4, this is due to the nonlinearity of nonnegative precipitation such that variability on average introduces more rainfall into desert and semidesert regions, in addition to the nonlinear rectification in the vegetation feedback. The shift of the maximum enhancement of vegetation due to climate variability shifts with the steepest response in  $V^*(P)$  from one model to

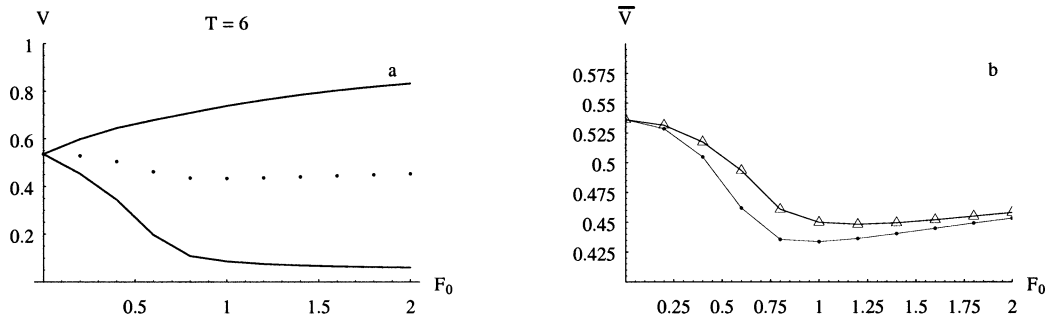


FIG. 13. As in Figs. 4a,b, but for the Miami model: vegetation as a function of forcing amplitude: (a)  $\bar{V}$  (average over a limit cycle; dotted line),  $V_{\max}$  (max value over a limit cycle; upper solid line), and  $V_{\min}$  (min value over a limit cycle; lower solid line); (b)  $\bar{V}$  as in (a) (linked dots) and  $\bar{V}$  for the case where the feedback from  $V$  is fixed at its steady-state value  $V = 0.54$  in Eq. (7) (linked triangles).

the other. The quantitative differences between the models are substantial and in application to more realistic modeling situations might result in these effects applying in slightly shifted geographic regions. Qualitatively, the two models are in agreement. In both the Miami model and the ZN model, climate variability acts to smooth out the vegetation and rainfall gradient at low to intermediate rainfall regions, and the largest impact is located around where the equilibrium vegetation response is strongest [the slope of  $V^*(P)$  is the largest].

When the periodic forcing is a small perturbation ( $F_0$  is small), the drift in the mean state can be analytically computed. In solving the slow dynamics (averaging) of a set of differential equations similar to ours, Dettinger (1997) and Dettinger et al. (2001, manuscript submitted to *J. Atmos. Sci.*, hereafter DVG) derived a general formula using a Lie averaging technique. Applying this general formula [Eqs. (4.6) and (4.7) of DVG] to our system of Eqs. (14) and (15), we obtain the equations governing the slow variation of  $V$  and  $P$ :

$$\frac{d\bar{V}}{dt} = 1 - \left( 1 + \frac{T^2 F_0^2}{16\pi^2} \right) e^{-\bar{P}} - \bar{V} \quad (16)$$

$$\bar{P} = P_1 + \mu \bar{V}. \quad (17)$$

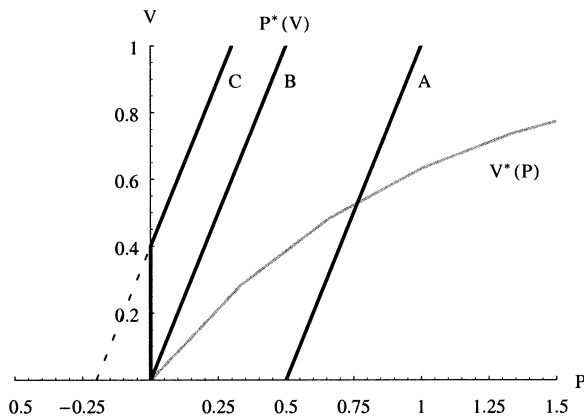


FIG. 14. As in Fig. 7, but for the Miami model.

Equation (16) differs from the original equation (14) by an additional term  $T^2 F_0^2 / 16\pi^2$  in  $V^*$ . This leads to a steady-state solution with smaller  $\bar{P}_s$  and  $\bar{V}_s$ . Because of the dependence of the slow dynamics on the squares of  $T$  and  $F_0$ , the nonlinear drift increases rapidly when forcing amplitude and period increase in the vicinity of  $T = 0$  and  $F_0 = 0$ .

### 7. Conclusions

In a simplified vegetation–atmosphere system, we have demonstrated the roles of vegetation feedback and climate variability in modifying the gradient from desert to forest, confirming the three-dimensional climate model results of ZN. The major points are the following:

- 1) A positive feedback from interactive vegetation leads to a wetter and greener state everywhere compared to a state without vegetation. As a result, at places with moderate precipitation (desert to savanna and woodland), the gradient in vegetation and rainfall is enhanced.
- 2) Climate variability, such as that arising from ocean variations, on average tends to reduce vegetation and precipitation in higher precipitation regions, while enhancing them in lower precipitation regions. As a result, the gradient in vegetation and rainfall becomes smoother, especially in the savanna regions.
- 3) Certain types of vegetation response curves and strong vegetation–atmosphere feedback can lead to the existence of multiple equilibria, which tend to enhance the vegetation gradient in savanna regions. But the multiple equilibrium states can be destroyed by the climate variability that smooths out this gradient.

It is of interest to note that the direct positive feedback effect from interactive vegetation is largely a linear effect, while the climate variability effect is rooted in the nonlinear response of vegetation to rainfall. The nonlinear behavior depends critically on the shape of the nonlinearity (a gentle rectifier effect). Present observational evidence is not sufficient to give us a more

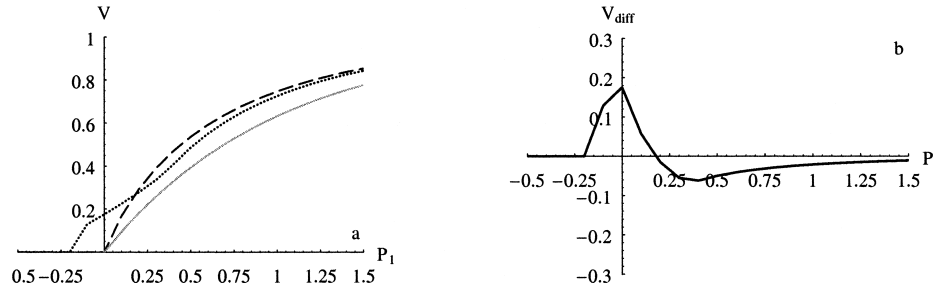


FIG. 15. As in Fig. 8, but for the Miami model.

precise constraint on the vegetation response curve. One of the reasons is that observations are the net result of all the possible influences discussed above. Thus, attempts to estimate the vegetation response curve from data implicitly assume that vegetation feedback effects do not alter the distribution significantly. Nonetheless, our conclusions apply qualitatively to both the Miami model (13) and the ZN model (3), with or without the existence of multiple equilibria. The nonlinearity acts in such a way that the system response is stronger at the positive phase than at the negative phase of the sinusoidal forcing, so a net gain is accumulated over a full forcing cycle.

Despite our discussions on the dependence on forcing frequency, we only considered periodic forcings in this paper. But natural climate variability has a broad spectrum that might better be modeled as a stochastic forcing. This can have significantly different effects than a simple superposition of periodic forcings in a nonlinear regime. Thus, this needs to be addressed in the future.

The models used in this study are simple, especially the vegetation models. For instance, a single vegetation timescale  $\tau_v$  does not realistically represent the rapid dying of vegetation under cold or drought stress, versus the slow growing process of trees. The seasonal cycle of subtropical wet and dry ecosystems corresponds to very different plant physiology and is not modeled here. Nonetheless, in the comprehensive coupled atmosphere–carbon model at the Hadley Centre, a shift in the vegetation distribution occurs as the result of El Niño–like variability generated by interactive ocean coupling (C. Jones and P. Cox, 2000, personal communication). Coupled vegetation–atmosphere models are often driven by climatological SST distribution (i.e., without climate variability arising from changes in SST) and the savanna regions are generally not well simulated (e.g., Foley et al. 1998). Our results suggest the need to include climate variability in such coupled models.

The interaction between vegetation and climate is becoming a focus of research. The results here demonstrate possible complications to this interaction due to nonlinearities in the coupled system: the positive vegetation feedback manifests itself more strongly in intermediate precipitation regions, leading to an increased desert–savanna gradient; but climate variability acts to reduce

this gradient in drier regions (Fig. 8). The modeling framework thus provides a prototype for ways in which vegetation plays an active role in modifying rainfall and vegetation distribution in a changing environment.

*Acknowledgments.* C. J. Tucker posed the question “what determines the desert–forest gradient?” We have also benefited from discussions with P. Cox, Y. Tian, and comments from M. Claussen and an anonymous reviewer. This research was supported by NSF Grants ATM-0196210, ATM-0082529, and NOAA Grant NA86GP0314.

## APPENDIX A

### Relation between the Nonlinear and the Linear Models and the Value of $\mu$

The dependence of response amplitude on forcing period is fundamentally a linear response, although modified by nonlinearity when the forcing is large. Linearize (1) and (2) at a point ( $P = P_G$ ):

$$\frac{dV'}{dt} = \frac{\alpha P' - V'}{\tau_v} \quad (\text{A1})$$

$$P' = \mu V' + F_0 e^{i\omega t}, \quad (\text{A2})$$

where  $\alpha = P_0^{-1} e^{-P_G/P_0}$ , so the solutions of Eqs. (A1)–(A2) for the oscillation amplitude and phase shift  $\phi_p$  relative to the forcing for  $P'$  are

$$\left| \frac{P'}{F_0} \right|^2 = \frac{1 + \omega^2 \tau_v^2}{(1 - \alpha\mu)^2 + \omega^2 \tau_v^2} \quad (\text{A3})$$

$$\tan(\phi_p) = -\frac{\alpha\mu\omega\tau_v}{1 - \alpha\mu + \omega^2\tau_v^2}. \quad (\text{A4})$$

For vegetation, the solutions are

$$\left| \frac{V'}{F_0} \right|^2 = \frac{\alpha^2}{(1 - \alpha\mu)^2 + \omega^2\tau_v^2} \quad (\text{A5})$$

$$\tan(\phi_v) = -\frac{\omega\tau_v}{1 - \alpha\mu}. \quad (\text{A6})$$

These dependences on normalized forcing frequency are shown in Fig. A1. An interesting feature is that the

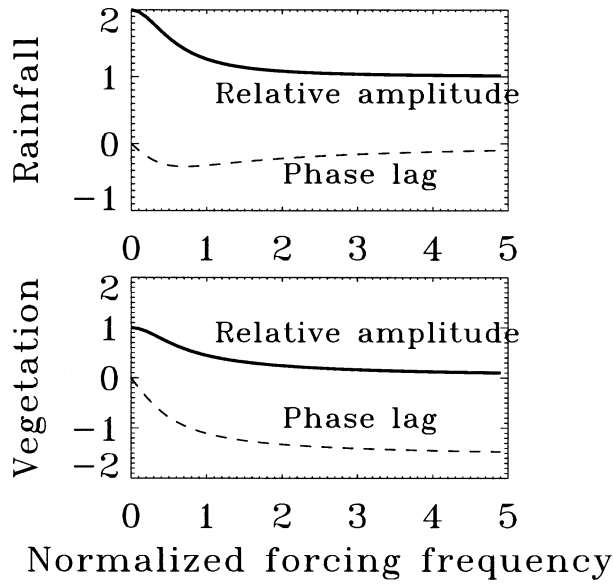


FIG. A1. Linear response to periodic forcing: amplitude and phase lag relative to the forcing for (a) precipitation  $P'$ , (b) vegetation  $V'$ .

phase lag in precipitation  $\phi_p$  is maximum at an intermediate value of  $F_0$ . This is because although feedback amplitude is large at low-frequency forcing ( $\omega\tau_v$  is small), the vegetation has sufficient time to adjust so it is in phase with the forcing. On the other hand, at high-frequency forcing ( $\omega\tau_v$  is large) the vegetation has no time to adjust to the forcing so the response amplitude is very small, despite that the phase lag is largest ( $-\pi$ ), so there is little feedback to precipitation. Thus the phase lag in precipitation is largest at intermediate values. This can lead to interesting lagged behavior on timescales comparable to the vegetation timescale. An example of this was discussed by ZNLT.

The above linearized equations are identical to the linear model used by ZNLT [their Eqs. (4) and (5)]. In order to see the vegetation feedback more closely, drop  $dV'/dt$  in (A1) and eliminate  $V'$  to obtain the steady-state solution for  $P'$ :

$$P' = \frac{F_0}{1 - \alpha\mu}. \quad (\text{A7})$$

This is a special case of the periodic forcing solution (A3) at  $\omega = 0$ . It is clear that the positive vegetation feedback effect depends both on how strongly vegetation responds to precipitation ( $\alpha$ ) and how precipitation responds to change in vegetation ( $\mu$ ). Note that the normalization  $\mu \rightarrow \mu/P_0$  in section 2 differs from  $\alpha\mu$  in (A1) and (A2) by a factor of  $e^{-P_G/P_0}$ , so the normalized  $\mu$  is somewhat larger than the value of  $\alpha\mu$  in ZNLT. Taking this factor into account by using  $P_G$  typical of savanna regions, we derived the normalized value  $\mu = 0.5$  in section 2, using the ensemble mean values for the Sahel from ZNLT (their Fig. 2; the ratio of AOLV and AOL).

## APPENDIX B

### An Analytical Example

The nonlinear drift and its effect on a system with multiple equilibria can be illustrated in a simpler system that is similar to the ZN model:

$$\frac{dy}{dt} = x - \frac{x^3}{3} - y \quad (\text{B1})$$

$$x = \mu y + F_0 \sin(\omega t). \quad (\text{B2})$$

Eliminate  $x$  in (B1) and collect terms according to  $\omega t$ :

$$\begin{aligned} \frac{dy}{dt} = & \left( \mu - 1 - \frac{\mu}{2}F_0 - \frac{\mu^3}{3}y^2 \right) y \\ & + \left( 1 - \mu^2y^2 - \frac{1}{4}F_0^2 \right) F_0 \sin(\omega t) \\ & + \frac{\mu}{2}F_0y^2 \cos(2\omega t) + \frac{1}{12}F_0^3 \sin(3\omega t). \end{aligned} \quad (\text{B3})$$

The system can be treated as the combination of a steady-state part (first term) and a sinusoidally forced (at three frequencies) part. Note that the oscillatory terms also involve terms nonlinear in  $y$ , so they can contribute to the steady solution. However, for high-frequency forcing, as discussed earlier, the oscillatory part of vegetation  $y$  has small amplitude because of the slow vegetation response, even for large forcing amplitude  $F_0$ . Thus, at sufficiently high-frequency forcing, the steady-state part of (B3) describes the slow dynamics. One can then set the first term to zero to yield approximate solutions for the steady states:

$$y_s = \begin{cases} 0 \\ \pm \sqrt{\frac{3}{\mu^3} \left( \mu - 1 - \frac{\mu}{2}F_0^2 \right)}. \end{cases} \quad (\text{B4})$$

There is only one solution  $y_s = 0$  when  $\mu \leq 1$ . Other

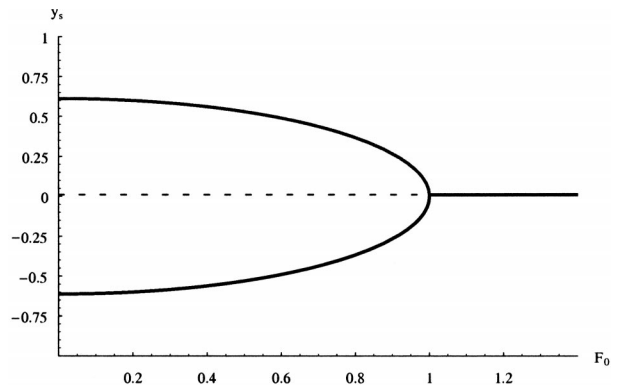


FIG. B1. Bifurcation diagram for the slow manifolds of the system in appendix B.

erwise multiple equilibria exist. Figure B1 shows the solution  $y_s$  as a function of  $F_0$  at  $\mu = 2$ . The steady-state solution of the slow manifolds exhibits a backward pitchfork bifurcation: there are three branches at small forcing, and one branch at large forcing, with the transition occurring at  $F_0 = \sqrt{[2(\mu - 1)]/\mu}$ . In the three-branch regime, the middle branch ( $y_s = 0$ ) is unstable, and the other two are stable. This is consistent with the numerical model results of ZN and the results in section 6. However, in Eq. (B1) the two branches are symmetric, and in the ZN model, the asymmetry makes the higher branch more stable than the lower branch (Fig. 9b), so that the “jump” occurs when forcing is large enough to kick the oscillatory orbit into the more stable one (Fig. 10). Introducing asymmetry of the form  $ax^2$  into (B1) modifies the pitchfork bifurcation. This has the effect that the upper branch continues to exist for values of  $F_0$  larger than the value where the lower branch disappears, providing a heuristic analogy in a univariate, steady-state system to the behavior seen in Fig. 10.

## REFERENCES

- Brovkin, V., M. Claussen, V. Petouknov, and A. Ganopolski, 1998: On the stability of the atmosphere–vegetation system in the Sahara/Sahel region. *J. Geophys. Res.*, **103**, 613–624.
- Charney, J. G., 1975: Dynamics of deserts and droughts in Sahel. *Quart. J. Roy. Meteor. Soc.*, **101**, 193–202.
- Claussen, M., 1994: On coupling global biome models with climate models. *Climate Res.*, **4**, 203–221.
- , V. Brovkin, A. Ganopolski, C. Kubatzki, and V. Petouknov, 1998: Modelling global terrestrial vegetation–climate interaction. *Philos. Trans. Roy. Soc. London*, **353B**, 53–63.
- Dettinger, M. D., 1997: Variations of continental climate and hydrology on diurnal-to-interdecadal time scales. Ph.D. thesis, Dept. of Atmospheric Sciences, University of California, Los Angeles, 240 pp.
- Dickinson, R. E., M. Shaikh, R. Bryant, and L. Graumlich, 1998: Interactive canopies for a climate model. *J. Climate*, **11**, 2823–2836.
- Ellis, J. E., and D. M. Swift, 1988: Stability of African pastoral ecosystems: Alternate paradigms and implications for development. *J. Range Manage.*, **41**, 450–459.
- Federov, A. V., and S. G. Philander, 2000: Is El Niño changing? *Science*, **288**, 1997–2002.
- Foley, J. A., I. C. Prentice, N. Ramankutty, S. Levis, D. Pollard, S. Sitch, and A. Haxeltine, 1996: An integrated biosphere model of land surface processes, terrestrial carbon balance, and vegetation dynamics. *Global Biogeochem. Cycles*, **10**, 603–628.
- , S. Levis, I. C. Prentice, D. Pollard, and S. L. Thompson, 1998: Coupling dynamic models of climate and vegetation. *Global Change Biol.*, **4**, 561–579.
- Folland, C. K., T. N. Palmer, and D. E. Parker, 1986: Sahel rainfall and worldwide sea temperatures, 1901–85. *Nature*, **320**, 602–607.
- Goward, S. N., and S. D. Prince, 1995: Transient effects of climate on vegetation dynamics—satellite observations. *J. Biogeogr.*, **22**, 549–564.
- Holdridge, L. R., 1947: Determination of world plant formations from simple climatic data. *Science*, **105**, 367–368.
- Ji, J.-J., 1995: A climate–vegetation interaction model: Simulating physical and biological processes at the surface. *J. Biogeogr.*, **22**, 445–451.
- Lieth, H., 1975: Modeling the primary productivity of the world. *Primary Productivity of the Biosphere*, H. Lieth and R. H. Whitaker, Eds., Springer-Verlag, 237–263.
- New, M., M. Hulme, and P. Jones, 1999: Representing twentieth-century space–time climate variability. Part I: Development of a 1961–90 mean monthly terrestrial climatology. *J. Climate*, **12**, 829–856.
- Nicholson, S. E., C. J. Tucker, and M. B. Ba, 1998: Desertification, drought, and surface vegetation: An example from the West African Sahel. *Bull. Amer. Meteor. Soc.*, **79**, 815–829.
- Pielke, R. A. Sr., R. Avissar, M. Raupach, A. J. Dolman, X. Zeng, and A. S. Denning, 1998: Interactions between the atmosphere and terrestrial ecosystems: Influence on weather and climate. *Global Change Biol.*, **4**, 461–475.
- Shugart, H. H., 1984: *A Theory of Forest Dynamics: The Ecological Implications of Forest Succession Models*. Springer-Verlag, 278 pp.
- Tucker, C. J., and S. E. Nicholson, 1999: Variations in the size of the Sahara Desert from 1980 to 1997. *Ambio*, **28**, 587–591.
- , H. E. Dregne, and W. W. Newcomb, 1991: Expansion and contraction of the Sahara Desert from 1980 to 1990. *Science*, **253**, 299–301.
- Woodward, F. I., 1987: *Climate and Plant Distribution*. Cambridge University Press, 174 pp.
- Xue, Y., and J. Shukla, 1993: The influence of land surface properties on Sahel climate. Part I: Desertification. *J. Climate*, **6**, 2232–2245.
- Zeng, N., and J. D. Neelin, 1999: A land–atmosphere interaction theory for the tropical deforestation problem. *J. Climate*, **12**, 857–872.
- , and —, 2000: The role of vegetation–climate interaction and interannual variability in shaping the African savanna. *J. Climate*, **13**, 2665–2670.
- , —, W. K.-M. Lau, and C. J. Tucker, 1999: Enhancement of interdecadal climate variability in the Sahel by vegetation interaction. *Science*, **286**, 1537–1540.